

Proper cytoskeletal architecture beneath the plasma membrane of red blood cells requires *Ttll4*

Faryal Ijaz^a, Yasue Hatanaka^b, Takahiro Hatanaka^b, Koji Tsutsumi^a, Takayuki Iwaki^c, Kazuo Umemura^c, Koji Ikegami^{a,b,*}, and Mitsutoshi Setou^{a,b,d,e,f,g,*}

^aDepartment of Cellular and Molecular Anatomy and International Mass Imaging Center, ^cDepartment of Pharmacology, and ^dPreeminent Medical Photonics Education & Research Center, Hamamatsu University School of Medicine, Hamamatsu, Shizuoka 431-3192, Japan; ^bMitsubishi Kagaku Institute of Life Sciences, Tokyo 194-8511, Japan†; ^eRiken Center for Molecular Imaging Science, Kobe, Hyogo 650-0047, Japan; ^fDepartment of Anatomy, University of Hong Kong, Hong Kong; ^gDivision of Neural Systematics, National Institute for Physiological Sciences, Okazaki, Aichi 444-8585, Japan

ABSTRACT Mammalian red blood cells (RBCs) circulate through blood vessels, including capillaries, for tens of days under high mechanical stress. RBCs tolerate this mechanical stress while maintaining their shape because of their elastic membrane skeleton. This membrane skeleton consists of spectrin-actin lattices arranged as quasi-hexagonal units beneath the plasma membrane. In this study, we found that the organization of the RBC cytoskeleton requires tubulin tyrosine ligase-like 4 (*Ttll4*). RBCs from *Ttll4*-knockout mice showed larger average diameters in smear test. Based on the rate of hemolysis, *Ttll4*-knockout RBCs showed greater vulnerability to phenylhydrazine-induced oxidative stress than did wild-type RBCs. Ultrastructural analyses revealed the macromolecular aggregation of cytoskeletal components in RBCs of *Ttll4*-knockout mice. Immunoprecipitation using the anti-glutamylated antibody GT335 revealed nucleosome assembly protein 1 (NAP1) to be the sole target of TLL4 in the RBCs, and NAP1 glutamylation was completely lost in *Ttll4*-knockout RBCs. In wild-type RBCs, the amount of glutamylated NAP1 in the membrane was nearly double that in the cytosol. Furthermore, the absence of TLL4-dependent glutamylation of NAP1 weakened the binding of NAP1 to the RBC membrane. Taken together, these data demonstrate that *Ttll4* is required for proper cytoskeletal organization in RBCs.

Monitoring Editor

Valerie Marie Weaver
University of California,
San Francisco

Received: Feb 8, 2016

Revised: Dec 8, 2016

Accepted: Dec 9, 2016

INTRODUCTION

Mammalian red blood cells (RBCs) maintain their shape despite being repeatedly exposed to mechanical stress while passing through capillaries. Beneath their plasma membrane, RBCs possess durable and elastic structures composed of spectrin-actin cytoskeleton (Lux, 2016). This membrane cytoskeleton is arranged as a quasi-hexagonal

lattice in which short actin filaments serve as a central joint bridging spectrin molecules (Liu *et al.*, 1987). This actin cytoskeleton is also associated with accessory proteins to form the extended spectrin-actin network (Fowler, 2013); these actin-associated proteins also control the size/length of the lattice structure (Moyer *et al.*, 2010). This cytoskeletal architecture is established before maturation of RBCs (Liu *et al.*, 2010), and the organization is maintained for tens of days. Disruption of the lattice structure leads to membrane instability and alterations of RBC shape, thereby impairing the physiological functions of RBCs (Mohandas and Gallagher, 2008). For instance, mice lacking the cytoskeletal protein 4.1R showed moderate hemolytic anemia with abnormal morphology of RBCs, reduced membrane stability (Shi *et al.*, 1999), and disrupted membrane cytoskeleton (Salomao *et al.*, 2008). In addition, the RBCs of tropomodulin 1-null mice exhibited increased osmotic fragility and mild spherocytic anemia with an abnormal membrane cytoskeleton (Moyer *et al.*, 2010). Furthermore, dysfunction of actin filaments results in altered membrane deformability (Gokhin *et al.*, 2015).

This article was published online ahead of print in MBOC in Press (<http://www.molbiolcell.org/cgi/doi/10.1091/mbc.E16-02-0089>) on December 14, 2016.

†The institute was closed in March 2009.

*Address correspondence to: Koji Ikegami (kikegami@hama-med.ac.jp), Mitsutoshi Setou (setou@hama-med.ac.jp).

Abbreviations used: KO, knockout; NAP1, nucleosome assembly protein 1; PHZ, phenylhydrazine; RBCs, red blood cells; TLL, tubulin tyrosine ligase-like.

© 2017 Ijaz *et al.* This article is distributed by The American Society for Cell Biology under license from the author(s). Two months after publication it is available to the public under an Attribution–Noncommercial–Share Alike 3.0 Unported Creative Commons License (<http://creativecommons.org/licenses/by-nc-sa/3.0>).

“ASCB®,” “The American Society for Cell Biology®,” and “Molecular Biology of the Cell®” are registered trademarks of The American Society for Cell Biology.

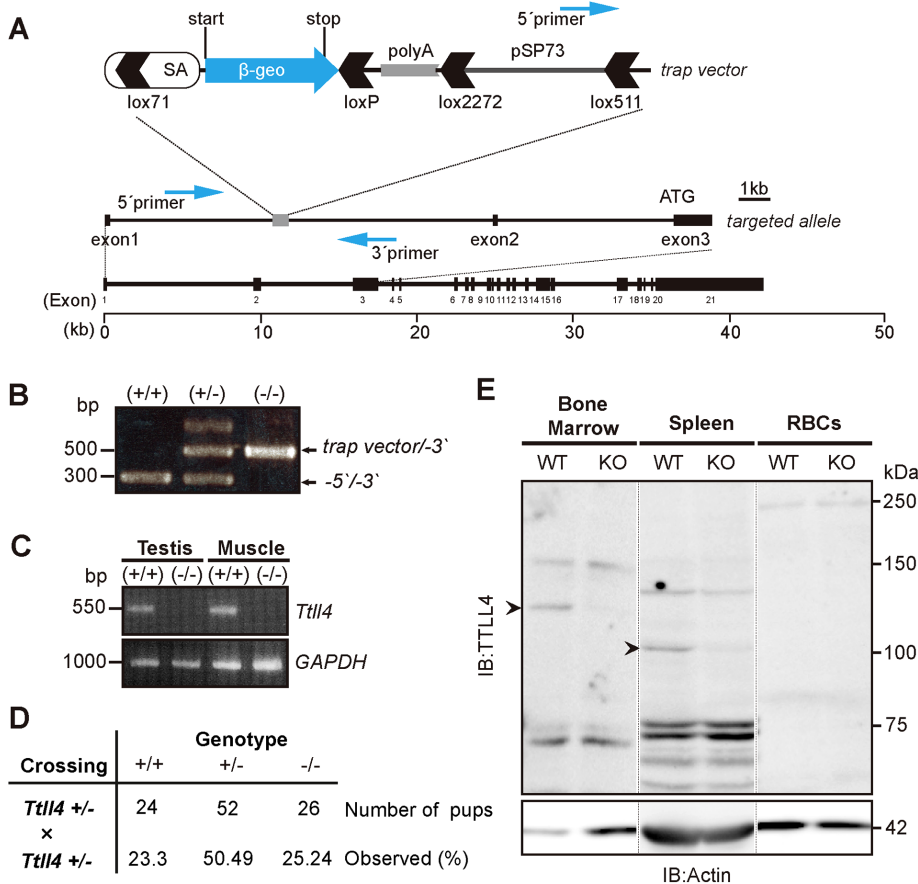


FIGURE 1: Disruption of *Ttl4* gene. (A) Schematic of *Ttl4* gene targeting. Arrows indicate primers for genotyping PCR. (B) Genotyping PCR showing *Ttl4* +/+ (wild type), +/- (heterozygote), and -/- (knockout). The wild-type allele was amplified as a 300-base pair fragment. The trapped allele was amplified as a 500-base pair fragment. (C) Total RNA prepared from wild-type (+/+) and knockout (-/-) testis and muscle was reverse-transcribed and then used for PCR amplification with primers specific for *Ttl4*. No amplification product (550 base pairs) for *Ttl4* was observed in knockout mice. Glyceraldehyde-3-phosphate dehydrogenase was used as a control. (D) Litter analysis showing the frequency of appearance of offspring of each genotype produced by interbreeding of *Ttl4*+/- mice. The sum of all the offspring produced from 21 matings for each genotype is shown. Mice 3–6 mo of age were used for mating. (E) Western blot analyses showing expression of TLL4 protein in different tissues. Actin was used as a loading control.

Tubulin tyrosine ligase-like 4 (TLL4) is a member of the tubulin tyrosine ligase-like (TLL) protein family. This family comprises 13 members, all of which contain an ~190-amino acid core TTL domain (Janke *et al.*, 2005; Ikegami *et al.*, 2006). TLL4 belongs to a sub-family of the TLL family along with eight other members, which catalyze glutamylation (Janke *et al.*, 2005; Ikegami *et al.*, 2006, 2007; Ikegami and Setou, 2010; van Dijk *et al.*, 2007). Glutamylation, covalent attachment of glutamic acids to the side chain of glutamic acid residues in target proteins (Edde *et al.*, 1990), occurs on tubulin and nontubulin proteins (Regnard *et al.*, 2000). Each of the TLLs involved in glutamylation has different preferences for the initiation or elongation of glutamylation, as well as different substrate specificities (Ikegami *et al.*, 2006; van Dijk *et al.*, 2007). TLL4 has strong glutamylation-initiating activity and broad substrate specificity, targeting various nontubulin proteins such as nucleosome assembly protein 1 (NAP1) and β -tubulin (van Dijk *et al.*, 2007, 2008). TLL4 is highly expressed in the bone marrow, a hematopoietic tissue (Ikegami *et al.*, 2006; Ye, Li, Yang, *et al.*, 2014). A recent study reported abnormal development of hematopoietic cells when TLL4 was

overexpressed in the bone marrow (Ye, Li, Yang, *et al.*, 2014).

In this study, we report the abnormal membrane cytoskeletal architecture in RBCs of *Ttl4*-knockout (KO) mice.

RESULTS

Blood cell counts in *Ttl4*-KO mice are not significantly different from those of wild-type controls

We obtained a candidate line of *Ttl4*-deficient mice in which an allele of *Ttl4* was trapped by a β -geo gene-trapping vector. Mouse *Ttl4* consists of 21 exons. In the candidate line of *Ttl4*-deficient mice, *Ttl4* was disrupted by insertion of the trapping vector between exons 1 and 2, which were placed upstream of exon 3 harboring the ATG start codon (Figure 1A). *Ttl4* heterozygotes were interbred to obtain *Ttl4*-null mice, and the genotypes were then determined by PCR (Figure 1B). Trapping of *Ttl4* in KO mice was confirmed by reverse transcription PCR with cDNA generated from total RNA extracted from the testis and muscle tissues of wild-type and *Ttl4*-null mice. The primers designed to amplify a 550-base pair region between exons 2 and 7 of *Ttl4* cDNA revealed a band of the expected size from wild-type (+/+) tissues but failed to detect a transcript band from a knockout (-/-) littermate (Figure 1C). Litter analysis revealed no gross abnormalities in litter size and the genotypic ratio of the pups (Figure 1D; $p = 0.795$ by chi-square test). Next we examined *Ttl4*-trapped homozygous mice using an anti-TLL4 polyclonal antibody raised against the C-terminal domain of TLL4. In the bone marrow, a 130-kDa protein band was detected in the wild-type control, whereas this band was absent in homozygous *Ttl4*-deficient mice (Figure 1E). In the spleen, a 100-kDa splice variant was expressed in wild-type animals, whereas its expression was completely absent in *Ttl4*-deficient mice (Figure 1E). These results demonstrated that mice containing *Ttl4* trapped by the vector were *Ttl4*-null, that is, *Ttl4*-KO animals. We failed to detect the expression of TLL4 in RBCs, even in wild-type mice (Figure 1E).

Because TLL4 is highly expressed in the bone marrow, we first examined the hematological parameters of the mice. The number of RBCs and reticulocytes was comparable between *Ttl4*-KO mice and wild-type controls, with no statistically significant differences detected (Table 1). The number of white blood cells was also comparable between *Ttl4*-KO mice and wild-type controls and did not show a significant difference (Table 1). The number of platelets in *Ttl4*-KO mice was not significantly different from that in wild-type mice (Table 1). Furthermore, there were no differences in other blood cell parameters, such as red cell distribution width, hemoglobin, hematocrit, mean cell volume, mean corpuscular hemoglobin, mean corpuscular hemoglobin concentration, and osmotic fragility between *Ttl4*-KO and wild-type mice (Table 1 and Supplemental Figure S1, A and B). Moreover, we detected no overt differences in

Hematological parameter	Wild type	<i>Ttll4</i> -KO
RBC count ($\times 10^4/\mu\text{l}$)	889.75 \pm 36.31	882 \pm 26.21
Reticulocytes (%)	2.44 \pm 0.44	3.36 \pm 0.61
WBC count ($\times 10^2/\mu\text{l}$)	129.2 \pm 19.33	133.7 \pm 28.8
PLT count ($\times 10^4/\mu\text{l}$)	42.675 \pm 10.57	49.1 \pm 23.48
RDW (%)	13.05 \pm 0.18	14 \pm 0.7
HGB (g/dl)	14.575 \pm 0.37	14.47 \pm 0.24
HCT (%)	42.375 \pm 0.89	43 \pm 0.59
MCV (fl)	47.75 \pm 1.07	48.85 \pm 1.41
MCH (pg)	16.45 \pm 0.35	16.45 \pm 0.28
MCHC (g/dl)	34.375 \pm 0.23	33.675 \pm 0.47

One-year-old female mice were used for analysis. Data are shown as mean \pm SEM of three individual experiments. For reticulocytes data are shown as mean \pm SEM of six individual experiments. RBC, red blood cell; WBC, white blood cell; PLT, platelets; RDW, red cell distribution width; HGB, hemoglobin; HCT, hematocrit; MCV, mean cell volume; MCH, mean corpuscular hemoglobin; MCHC, mean corpuscular hemoglobin concentration.

TABLE 1: Comparison of hematological analysis between wild-type and *Ttll4*-KO mice.

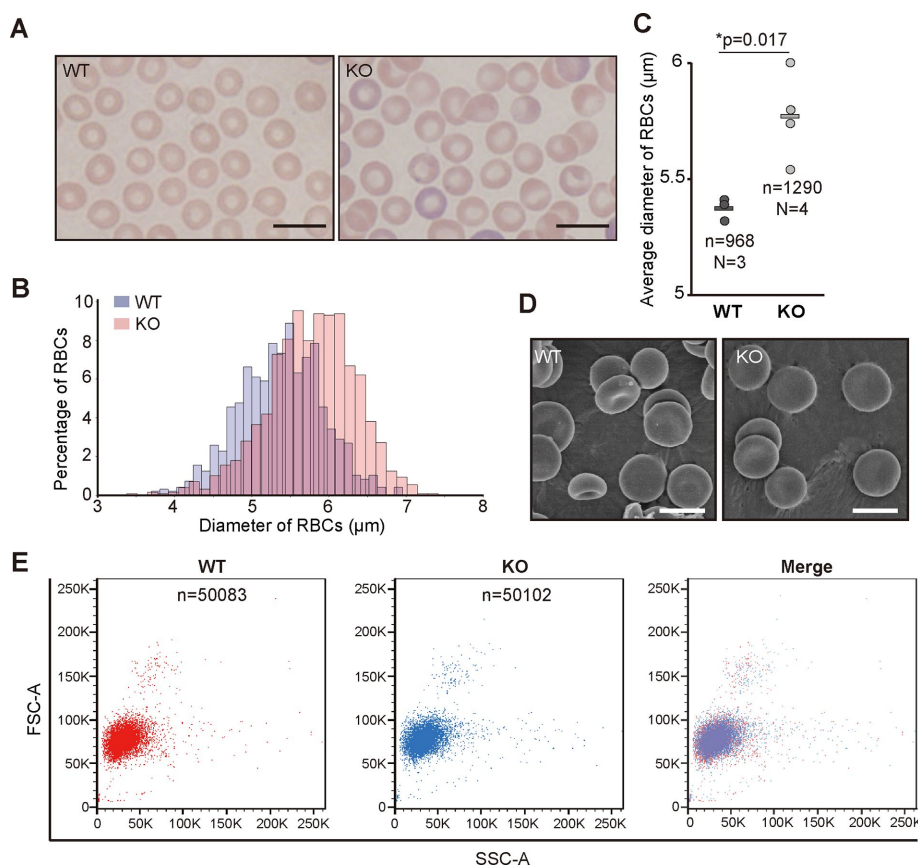


FIGURE 2: RBC morphology of wild-type and *Ttll4*-KO mice under normal conditions. (A) Giemsa-stained RBCs. Scale bar, 10 μm . (B) Histogram showing the distribution of RBC diameters. The number of RBCs tested: 968 from three independent wild-type animals and 1290 from four independent *Ttll4*-KO mice. (C) Comparison of average diameter of RBCs in individual animals of wild-type ($N = 3$) and *Ttll4*-KO ($N = 4$) mice. Data are shown as mean \pm SEM ($*p < 0.05$). (D) Scanning electron micrographs of RBCs of wild-type and *Ttll4*-KO mice. Scale bar, 4 μm . (E) Flow cytometry features of wild-type and *Ttll4*-KO RBCs. Mice 8–12 mo of age regardless of the sex were used for each experiment.

the ektacytometry analysis of *Ttll4*-KO RBCs and wild-type RBCs. The deformability index of *Ttll4*-KO RBCs was comparable to that of wild-type RBCs (Supplemental Figure S1C).

Ttll4-KO RBCs have larger average diameters in the smear test

In Giemsa-stained blood cell smears, we observed an overt difference in the morphology of RBCs between *Ttll4*-KO and wild-type mice. The *Ttll4*-KO RBCs appeared larger than wild-type RBCs (Figure 2A). A histogram of the diameters of RBCs revealed higher values for the KO mice than for the wild type (Figure 2B). The average diameter of *Ttll4*-KO RBCs was significantly larger than that of wild-type RBCs (5.77 μm in *Ttll4*-KO vs. 5.37 μm in wild type; $p = 0.017$; Figure 2C). In addition, the average diameters of RBCs calculated from each individual *Ttll4*-KO mouse showed much higher variance than those of wild-type mice: the SD was 0.19 μm for *Ttll4*-KO versus 0.05 μm for wild type; the coefficient of variance was 0.03 for *Ttll4*-KO versus 0.01 for wild type (Figure 2C).

To analyze the detailed morphology of *Ttll4*-KO and wild-type RBCs, we observed glutaraldehyde-fixed RBCs by scanning electron microscopy (SEM). Surprisingly, the overall morphology of *Ttll4*-KO RBCs was comparable to that of wild-type RBCs (Figure 2D). We further examined the sizes of RBCs using fluorescence-activated cell sorting (FACS) analysis after labeling intact RBCs with fluorescent anti-Ter119 antibodies. RBC sizes were comparable between *Ttll4*-KO and wild-type mice, similar to the SEM results (Figure 2E).

Ttll4-KO RBCs are vulnerable to oxidative stress

To further determine whether the integrity of RBC morphology under stressful conditions depends on the TLL4 enzyme, we prepared a hemolytic anemic mouse model of both wild-type and *Ttll4*-KO mice by injecting 20 mg/kg

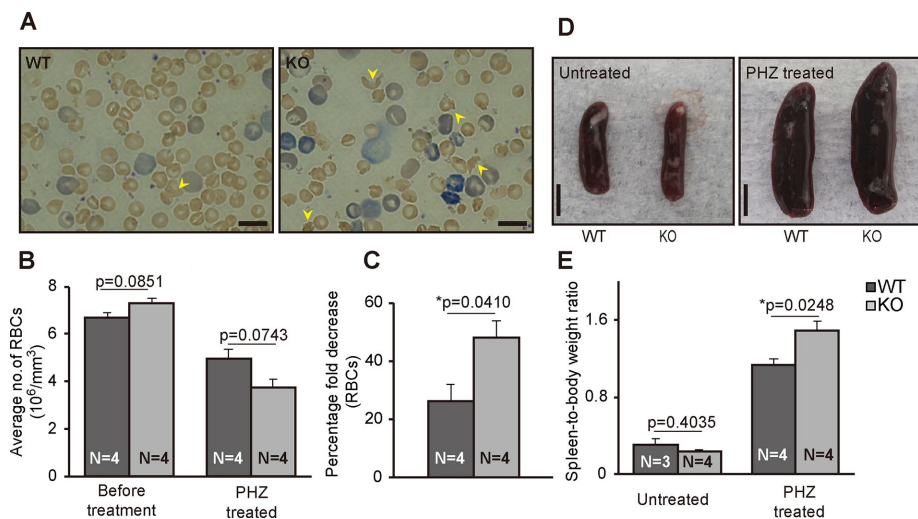


FIGURE 3: RBC morphology of wild-type and *Ttll4*-KO mice under oxidative stress. (A) Giemsa-stained RBCs 2 d after PHZ treatment. Scale bar, 10 μ m. Arrowheads, lysed RBCs. (B) Quantitative analysis of the average number of RBCs before and after PHZ treatment. (C) Fold-percentage decrease in the number of RBCs by PHZ treatment in individual wild-type and *Ttll4*-KO mice. Data are shown as mean \pm SEM of fold-percentage decrease (4 mice per group; * $p < 0.05$). (D) Morphology of the spleen of untreated and PHZ-treated wild-type and *Ttll4*-KO mice. Scale bar, 1 cm. (E) Quantitative analysis of relative weight of spleen to body weight (spleen-to-body weight ratio). Data are shown as mean \pm SEM (untreated: wild type $N = 3$, *Ttll4*-KO $N = 4$; PHZ treated: $N = 4$ for both wild type and *Ttll4*-KO; * $p < 0.05$). Mice 8–12 mo of age regardless of the sex were used for each experiment.

phenylhydrazine (PHZ) into the mouse peritoneal cavity and observed the changes in RBCs 2 d later. Under PHZ-induced oxidative stress, *Ttll4*-KO mice showed remarked hemolysis, as observed in Giemsa-stained blood smears (Figure 3A, arrowheads). The number of RBCs tended to be lower in PHZ-treated *Ttll4*-KO animals ($3.77 \times 10^6/\text{mm}^3$) than in PHZ-treated wild-type animals ($4.61 \times 10^6/\text{mm}^3$; Figure 3B).

Given that the number of steady-state RBCs in *Ttll4*-KO mice was slightly higher than that in wild-type mice (Figure 3B), we calculated and compared the percentage fold decrease of RBCs after PHZ treatment. The fold decrease was ~50% in *Ttll4*-KO mice, whereas that in wild-type mice was ~29%, showing a significant difference (Figure 3C).

Finally, we examined the effect of PHZ treatment on spleen morphology. Pronounced splenomegaly was observed in *Ttll4*-KO mice under PHZ administration (Figure 3D). In addition, the weight of the spleen relative to the body weight of *Ttll4*-KO mice was 1.3-fold higher than that for wild-type mice under PHZ administration (Figure 3E).

Ttll4-KO RBCs have abnormal cytoskeletal architecture beneath the plasma membrane

The foregoing findings prompted us to investigate the organization of the membrane skeleton of RBCs for underlying defects. We used transmission electron microscopy (TEM) to visualize the membrane skeleton of RBC ghosts that were fixed with glutaraldehyde, negatively stained with uranyl acetate, and attached to copper grids coated with Formvar and carbon. TEM revealed a noticeable difference in the meshwork between *Ttll4*-KO and wild-type RBCs. Magnified photographic images revealed that the meshwork had uncharacteristic “holes” in the membrane skeleton in *Ttll4*-KO RBCs (Figure 4A). However, individual actin-spectrin lattices were not visible in the electron micrographs. On average, there were 9.5 holes/ μ m

μ m in *Ttll4*-KO RBCs, whereas the wild-type RBC membrane skeleton had a higher density of holes, with 12.6 holes/ μ m (Figure 4B).

Glutamylated NAP1 is concentrated in the RBC membrane and is lost in *Ttll4*-KO RBCs

We analyzed whole RBC lysates prepared from wild-type and *Ttll4*-KO mice by Western blot analysis with a monoclonal antibody (mAb) specific for glutamylation—GT335—in order to identify which protein(s) were glutamylated in a TLL4-dependent manner in RBCs. We detected a ~60-kDa protein as the sole major band in whole lysates of wild-type RBCs; this band disappeared in *Ttll4*-KO samples (Figure 4A and Supplemental Figure S2). We next performed immunoprecipitation to determine which protein was detected with the glutamylation-specific mAb GT335. The ~60-kDa protein that was immunoprecipitated with the mAb GT335 from wild-type RBC lysates was detected using an anti-NAP1 antibody (Figure 5B). No NAP1 was precipitated from the *Ttll4*-KO RBC lysate with the mAb GT335 (Figure 5B). In addition, the mAb GT335 recognized NAP1 immunopurified from the wild-type RBC lysate

but did not detect the protein purified from the *Ttll4*-KO RBC lysate (Figure 5C). Of note, a slight decrease in the molecular weight of NAP1 was observed in *Ttll4*-KO RBC samples (Figure 5, B and C).

We next analyzed the intracellular localization of glutamylated NAP1 in RBCs. Immunocytochemical analyses showed that total NAP1 was localized predominantly in the cytosol in both wild-type and *Ttll4*-KO RBCs (Figure 5D). Thus we fractionated the cytosolic and membranous components of RBCs and analyzed these samples by Western blotting. We loaded 80-fold more protein from the membranous fraction than from the cytosolic fraction to obtain nearly comparable NAP1 levels in both the membranous and cytosolic fractions, given the predominant localization of NAP1 in the RBC cytosol. In wild-type RBCs, the band for glutamylated NAP1 appeared to be more intense in the membranous fraction than in the cytosolic fraction (Figure 5E). Quantitative and statistical analyses of the Western blotting results showed that the glutamylation level of NAP1 in the membranous fraction was nearly double that in the cytoplasmic fraction (1.39 vs. 0.73 arbitrary units; Figure 5F). Glutamylated NAP1, which was normally concentrated in the membrane, was completely lost in the *Ttll4*-KO RBC membrane (Figure 5E).

Glutamylated NAP1 is important for its binding with the RBC membrane

Coomassie blue-stained gels and Western blot analysis of RBC Mg²⁺ ghosts and the Triton X-100-insoluble membrane skeleton revealed normal amounts of the major proteins α -spectrin, β -spectrin, band 3, protein 4.1, protein 4.2, and actin in the *Ttll4*-KO RBC membrane (Figure 6, A and B). Moreover, levels of the actin-binding proteins α -adducin, β -adducin, tropomodulin 1, and tropomyosin remained nearly unchanged in the *Ttll4*-KO RBC membrane (Figure 6, A and B). NAP1 was detected in both Mg²⁺ ghosts and Triton-insoluble membrane skeleton fractions of both wild-type and *Ttll4*-KO RBCs (Figure 6A).

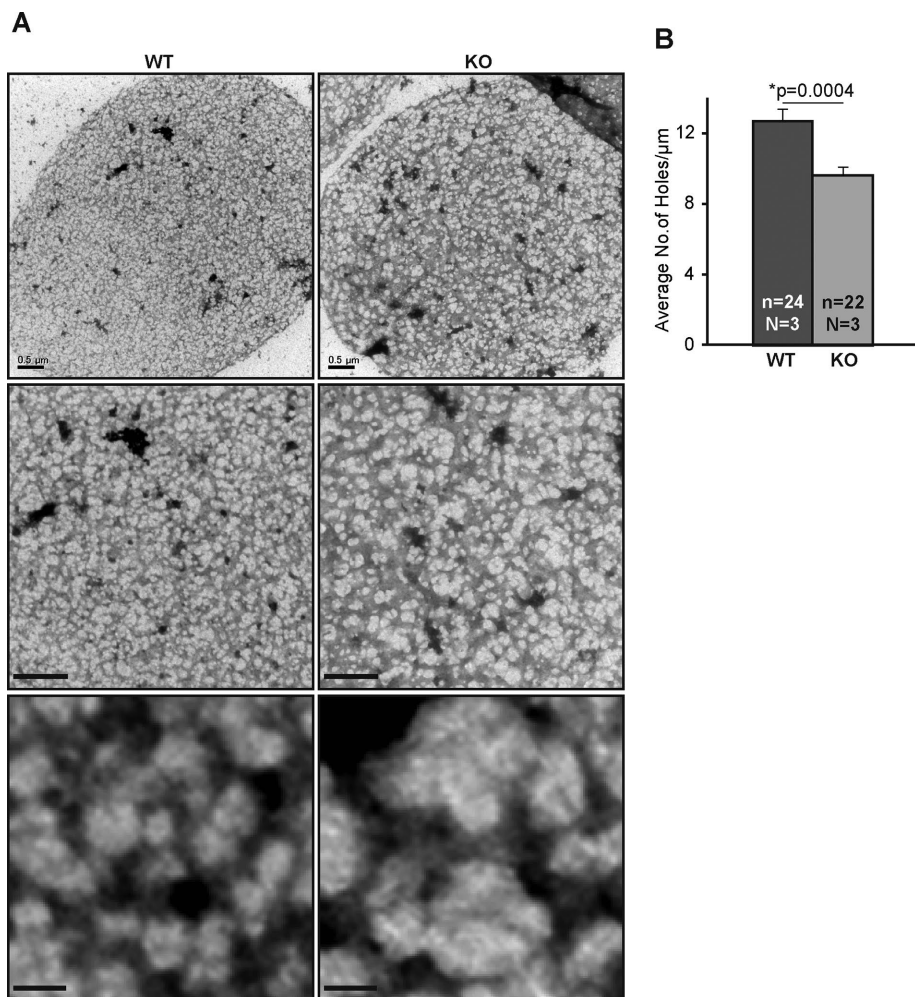


FIGURE 4: RBC membrane cytoskeleton displays abnormal macromolecular aggregation in the absence of *Ttl4*. (A) Electron micrographs of unspread RBC membrane ghosts from wild-type and *Ttl4*-KO mice. Top, low-power microscopic images showing entire membrane ghosts; scale bar, 500 nm. Middle, high-power microscopic images of the samples shown at top; scale bar, 250 nm. Bottom, magnified images of the high-power images showing meshwork with irregular holes and normal holes in *Ttl4*-KO and wild-type RBC membrane ghosts, respectively; scale bar, 15 nm. (B) Quantitative analysis of the number of holes on a scanned line. Data are shown as mean \pm SEM (wild type: 24 cells from four independent mice; *Ttl4*-KO: 22 cells from four independent mice; * $p < 0.05$). Mice 8–12 mo of age regardless of the sex were used for each experiment.

To determine the effect of TTLL4-mediated glutamylation of NAP1 on its interaction with membrane proteins, we incubated wild-type and *Ttl4*-KO Mg^{2+} membrane ghosts in increasing concentrations of KCl and then evaluated NAP1 levels in both the supernatant and the remaining membrane pellet fractions. The total amounts of NAP1 were similar in the wild-type and *Ttl4*-KO RBC membranes (Figure 6, C, left, and D). The levels of NAP1 released from the wild-type and *Ttl4*-KO RBC membranes into the supernatant increased, depending on the salt concentration; NAP1 release was lower at lower salt concentrations and higher at higher salt concentrations (Figure 6, C and E). In addition, at 210 and 310 mM KCl, more NAP1 was released into the supernatant from the *Ttl4*-KO RBC membrane than from the wild-type RBC membrane (Figure 6, C, middle, and E).

DISCUSSION

RBCs of *Ttl4*-KO mice appeared normal under aldehyde-fixed or intact conditions but were flattening and showed a higher variance of mean diameters in the smear test. We inferred that the observed

changes in the RBC phenotypes in smear were due to the morphological vulnerability of *Ttl4*-KO RBCs under stress rather than actual differences in the sizes of RBCs. Similarly, *Ttl4*-KO RBCs were more vulnerable than control RBCs to hemolysis caused by PHZ-induced high oxidative stress. One plausible explanation for this observation is that *Ttl4*-KO RBC membrane proteins may undergo more oxidative cross-linking. This enhanced oxidative sensitivity may be due to primary structural/functional defects in the membrane cytoskeleton of *Ttl4*-KO RBCs (Becker *et al.*, 1987; Fibach and Rachmilewitz, 2008). Consistent with these results, ultrastructural analyses revealed uncharacteristic holes beneath the plasma membrane of RBCs in *Ttl4*-KO mice, suggesting macromolecular aggregation/instability of cytoskeletal components, presumably caused by primary structural/functional defects in *Ttl4*-KO RBCs. These results appeared to be corroborated by prior evidence showing that defective cytoskeleton proteins result in cytoskeletal protein aggregation (Kalfa *et al.*, 2006; Chen *et al.*, 2007).

The abnormal macromolecular aggregation detected in the *Ttl4*-KO RBC cytoskeleton could be explained in terms of inappropriate molecular interactions. Electrostatic interactions determine the adhesion of the skeleton to the substrate, and tighter binding prevents the cytoskeletal components from moving together and condensing (Swihart *et al.*, 2001). On the basis of this background, we hypothesize that *Ttl4*-KO RBC cytoskeletal proteins may have altered ionic interactions, preventing their tight binding to the substrate and resulting in aggregation of the components. Glutamylated NAP1 could be responsible for maintaining proper ionic interactions among proteins, and the lack of glutamylation on NAP1 disrupted this balance (Figure 6, C and E). More discussion on salt-induced NAP1 release is presented later.

Our data showed that NAP1 was the only glutamylated protein in whole RBC lysates (Figure 5A). These data indicate that NAP1 is either the only substrate of the TTLL4 enzyme in mature RBCs or that other glutamylated substrates are present below the detection limit of the mAb GT335. Our results showing the higher levels of glutamylated NAP1 in the RBC membrane and the morphology of the cytoskeleton suggest that glutamylated NAP1 may have a role in cytoskeletal protein dynamics through its chaperone activity. NAP1 interacts with a wide array of proteins involved in many cellular processes, including roles related to histone chaperone characteristics and exchange of proteins (Zlatanova *et al.*, 2007). In *Xenopus laevis* eggs, NAP1 chaperone activity is important for normal binding and deposition of the linker histone H1M to chromatin; glutamylation is essential for H1M dynamics in the cell cycle (Miller and Heald, 2015). TTLL4-mediated glutamylation indeed modulates the chaperone function of

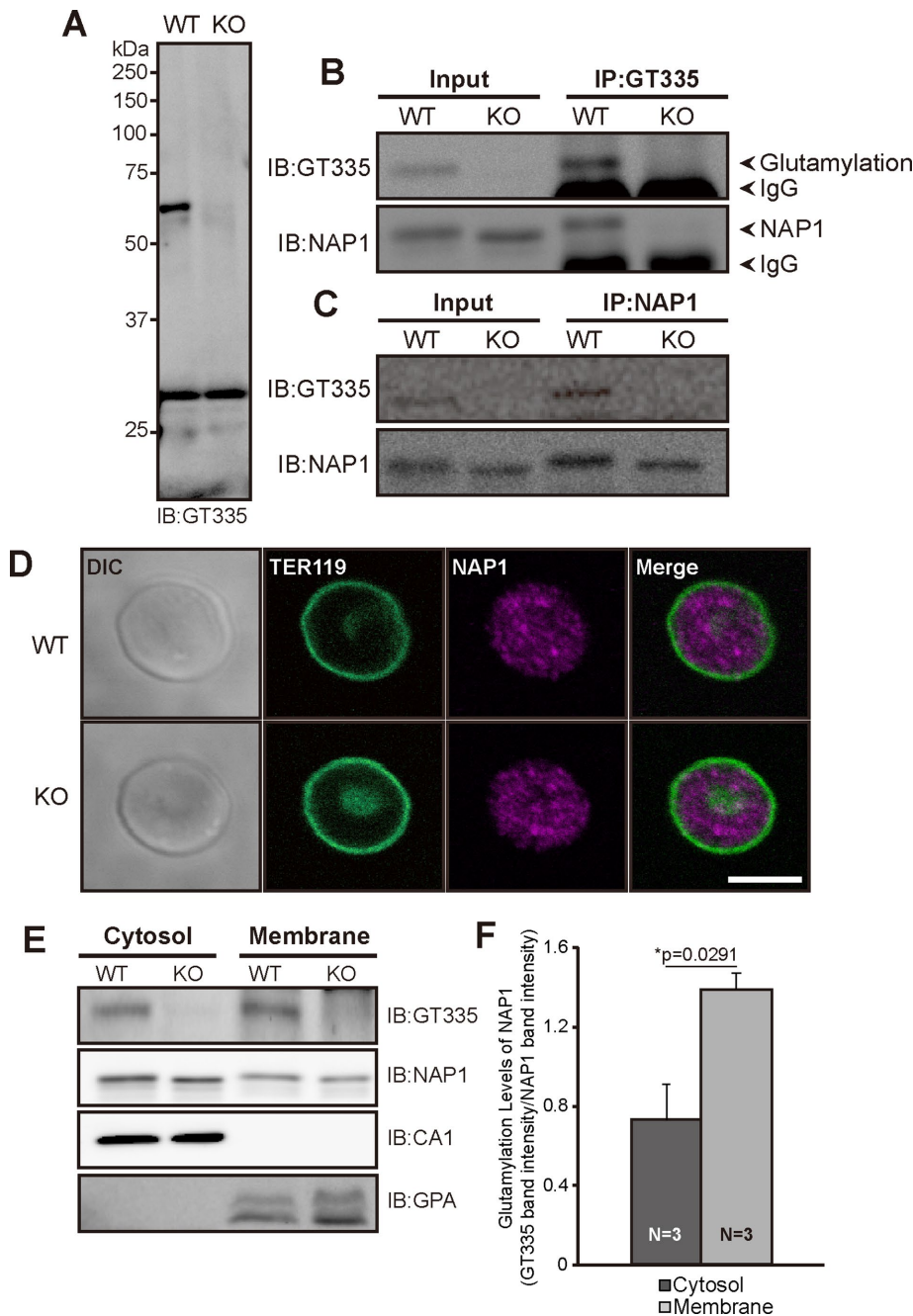


FIGURE 5: TLL4 modifies NAP1 in RBCs. (A) Immunoblot showing 60-kDa glutamylated protein in whole red blood lysate of wild-type and *Tll4*-KO mice. mAb GT335 was used to detect glutamylation. (B) Immunoblots (IB) after immunoprecipitation (IP) of 60-kDa glutamylated protein from RBC lysate performed with GT335 antibody. (C) Proteins immunoprecipitated with anti-NAP1 antibody. (D) Confocal microscopy images after immunohistochemistry showing NAP1 (magenta) in RBCs. TER-119 (green) is the erythroid marker. Scale bar, 5 μ m. (E) Immunoblotting analysis of levels of glutamylated NAP1 in cytosolic and membrane fraction of wild-type and *Tll4*-KO RBCs. Carbonic anhydrase1 (CA1) and glycophorin A (GPA) were used as cytosolic and membrane markers, respectively. (F) Quantification of glutamylation levels of NAP1 as described in E. Data are shown as mean \pm SEM (three mice per group; * $p < 0.05$). Mice 8–12 mo of age regardless of the sex were used for each experiment.

nucleoplasm (Onikubo *et al.*, 2015). In addition, some RBC cytoskeletal proteins are dynamic, and interaction and exchange of protein subunits occurs at the cytoskeleton (Gokhin *et al.*, 2015). Thus glutamylated NAP1 may be required for proper deposition of these exchange factors at the membrane cytoskeleton.

megakaryocyte-erythroid progenitor cells in the bone marrow (Vannucchi *et al.*, 2000) and show similarities in differentiation, cytology, and homeostatic regulation (Kaushansky, 2008; Klimchenko *et al.*, 2009). Other possibilities include that TLL4-mediated glutamylation of PELP1, a chromatin remodeler, affects the epigenetic

The levels of glutamylated and nonglutamylated NAP1 released from the RBC membrane into the supernatant were increased, depending on the salt concentration, demonstrating that the interaction between NAP1 and the RBC membrane is electrostatic, irrespective of the glutamylation state. Under higher salt concentrations, the electrostatic interaction weakens; for example, the NAP1–histone complex dissociated as the concentration of sodium chloride increased (Park and Luger, 2006). In addition, nonglutamylated NAP1 was more easily released into the supernatant than glutamylated NAP1 after incubation in increasing salt concentrations (Figure 6, C and E), demonstrating that the lack of TLL4-dependent glutamylation weakens NAP1 binding with the RBC membrane. The extra negative charge created by glutamylation on NAP1 may provide an acidic binding surface for other RBC cytoskeletal proteins. For NAP–histone binding, the acidic binding surface of the NAP1 dimer asymmetrically engages a single H2A–H2B heterodimer (Aguilar-Gurrieri *et al.*, 2016) and prevents nonspecific (*i.e.*, nonnucleosomal) histone–DNA interactions (Andrews *et al.*, 2010). Of all the cytoskeletal proteins, only actin has been shown to bind NAP1 (Seebart *et al.*, 2010). The acidic binding surface on NAP1 could be a possible attachment site for actin, and TLL4-dependent glutamylation may affect the ability of NAP1 to bind actin or other skeleton proteins, potentially acting as a linker between actin and other proteins. Moreover, the stability of actin from RBCs may be altered in the absence of NAP1 glutamylation because the extra negative charge on NAP1 contributes to the stability of the NAP1–protein complex (Park and Luger, 2006).

We cannot rule out the possibility that a lack of TLL4 in the bone marrow may affect the development and maturation of RBCs because TLL4 is highly expressed in this tissue (Figure 1E; Ikegami *et al.*, 2006; Ye, Li, Yang, *et al.*, 2014). TLL4-mediated glutamylation of MAD2 is responsible for maturation of megakaryocytes in the bone marrow (Ye, Li, Yang, *et al.*, 2014), and maturation of platelets in the peripheral blood also requires intense cytoskeletal reorganization (Chen *et al.*, 2007; Italiano *et al.*, 2007). Although platelets and erythrocytes have different functions, both megakaryocytes and erythroid lineages proliferate from common

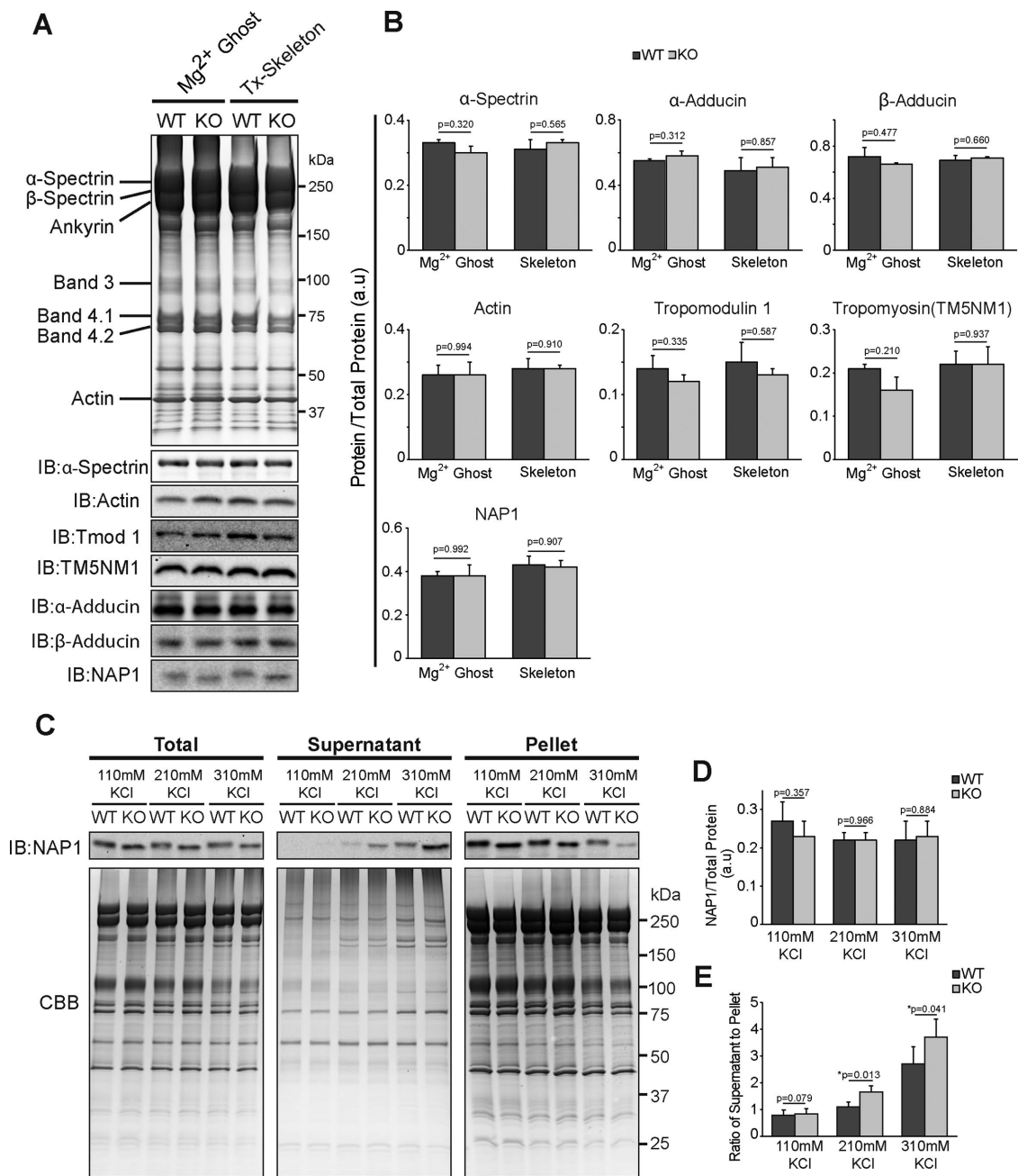


FIGURE 6: TLL4-mediated glutamylation of NAP1 controls NAP1 interaction with RBC membrane. (A) Coomassie-stained gel and immunoblots showing the comparison of Mg²⁺ ghosts and Triton-insoluble cytoskeleton protein composition in wild-type and *Ttll4*-KO RBCs. Coomassie brilliant blue (CBB) staining served as a loading control for the normalization of protein levels. (B) Quantification of levels of α -spectrin, α -adducin, β -adducin, actin, tropomodulin 1, tropomyosin (TM5NM1), and NAP1 proteins in Mg²⁺ ghosts and Triton-insoluble cytoskeleton of RBCs as described in A. Data are shown as mean \pm SEM (three mice per group; * $p < 0.05$). (C) Immunoblots showing the levels of NAP1 from wild-type and *Ttll4*-KO RBC membranes in different salt concentrations. CBB staining served as a loading control for the normalization of NAP1 levels. (D) Quantification of levels of glutamylated and nonglutamylated NAP1 in total membrane fraction as described in C. Data are shown as mean \pm SEM (three mice per group; * $p < 0.05$). (E) Quantification of levels of glutamylated and nonglutamylated NAP1 in supernatant and remaining membrane pellet as a ratio of supernatant to the pellet as described in C. Data are shown as mean \pm SEM (three mice per group; * $p < 0.05$, paired t test). Mice 8–12 mo of age regardless of the sex were used for each experiment.

regulation of RBC development or the expression of protein components of RBC membranes (Kashiwaya *et al.*, 2010).

Under steady-state conditions, the lack of *Ttll4* does not severely affect the function of RBCs, indicating that *Ttll4* plays a unique but subtle role in RBCs; further studies are needed to fully elucidate the

functions of TLL4 in this context and experimentally demonstrate how TLL4-mediated glutamylation of NAP1 is important for RBCs. Thus the next step in determining whether NAP1 binds to actin and other membrane skeleton proteins, potentially acting as a linker between actin and other proteins, may involve identifying the NAP1

binding partners in the RBCs. Knowing the exact localization of glutamylated NAP1 on the membrane cytoskeleton through superresolution microscopy (Qu, Hahn, et al., 2017) and/or electron microscopy would further help to identify the role of glutamylated NAP1 in RBCs. In addition, recombinant NAP1 proteins and binding assays (Miller and Heald, 2015) could be used to check whether glutamylation affects the ability of NAP1 to bind to RBC membrane proteins. In addition, measuring the amount of actin in the supernatant after Triton X-100 extraction of whole RBCs in combination with FRAP analysis (Gokhin et al., 2015) should confirm the involvement of glutamylated NAP1 in the interaction and exchange of actin polymerization and depolymerization factors at the RBC cytoskeleton. Clearly, investigation of the proposed mechanisms would be vital for resolving the role of TLL4-dependent glutamylation of NAP1 in RBCs.

In conclusion, we showed that proper RBC cytoskeletal organization requires the presence of the glutamylation-initiating glutamic acid ligase gene *Tll4*.

MATERIALS AND METHODS

Antibodies

Anti-TLL4 antibody was raised in guinea pigs immunized with the glutathione S-transferase (GST)-fused C-terminal domain of TLL4 (TLL4 C'50AA). The polyclonal anti-Tll4 antibody was purified using a column filled with the GST-tagged TLL4 C-terminal domain (TLL4 C'50AA). The fractionated anti-TLL4 antibody was further precleared against TLL4 KO tissue lysates. The mAb 4A8 for NAP1 was a kind gift from Yukio Ishimi (Ibaraki University, Mito, Japan). Other antibodies used in this study were as follows: polyglutamylation (mouse mAb GT335; AG-20B-0020-C100; AdipoGen, San Diego, CA); NAP1LI (rabbit polyclonal; ab33076; Abcam, Cambridge, United Kingdom); glycophorin A (mouse mAb; ab129024; Abcam); carbonic anhydrase1 (rabbit polyclonal; ab86280; Abcam); tropomyosin (mouse monoclonal; ab7785; Abcam); tropomodulin1 (mouse monoclonal; ab119025; Abcam); α -adducin (rabbit polyclonal; A303-713A; Bethyl Laboratories, Montgomery, TX); β -adducin (rabbit polyclonal; A303-741A; Bethyl); Ter119 (Alexa Fluor 488 anti-mouse TER-119/erythroid cells antibody; 116215; BioLegend, San Diego, CA); actin (rabbit polyclonal; A2066; Sigma-Aldrich, St. Louis, MO); spectrin β -chain (rabbit polyclonal; ABT185; Millipore, Billerica, MA), Alexa fluorophore-conjugated secondary antibodies for immunofluorescence (Invitrogen, Carlsbad, CA), and horseradish peroxidase-conjugated secondary antibodies for Western blot analysis (Jackson Immuno Research Laboratories, West Grove, PA).

Mice

All experiments and treatments in mice were approved by the Institutional Animal Care and Use Committee at the Hamamatsu University School of Medicine. *Tll4* allele-trapped mice were purchased from Trans Genic (Kobe, Japan) and mated with wild-type C57BL/6J mice for at least 10 generations. *Tll4*^{-/-}, *Tll4*^{+/-}, and wild-type littermates were obtained from heterozygous mating. Mice 8–12 mo of age, regardless of the sex unless otherwise specified, were used for each experiment. The bone marrow and spleen were dissected from adult C57BL/6J wild-type and *Tll4*^{-/-} mice. The organs were homogenized in lysis buffer (50 mM Tris-Cl, pH 7.5, 1% Triton X-100). For the hemolytic anemia model, adult C57BL/6J and *Tll4*^{-/-} mice were injected with 20 mg/kg PHZ (Sigma-Aldrich; 114715) every 24 h for two consecutive days. Mice were killed at 48 h after injection, and hematological parameters were analyzed.

Genotyping of progenies by PCR

Genomic DNA was prepared from 4- to 5-mm tail samples and then used for genotyping by PCR. Oligonucleotides used were 5'-TTCTGTAGCTGGGCTTATT-3' as the forward primer for the wild-type allele, 5'-AATCCCATGGTCCCACAAA-3' as the forward primer for the trap vector, and 5'-CGGTGAAACCTCGACACA-3' as the reverse primer for both the wild-type and trapped alleles.

Reverse transcription PCR

Total RNA was extracted from the testis and muscle tissues. Next 1 μ g of RNA per sample was reverse-transcribed into cDNA with RTace (Toyobo, Osaka, Japan) and oligoT15 primer. The resulting cDNA was amplified with primers specific for *Tll4*: forward, 5'-TATCTCGGAAGTGTGTGGATTGA-3', and reverse, 5'-GAATGACCTGAATCCAATGC-3' and AmpliTaq Gold.

Blood collection and hematology analyses

Whole blood (200 μ l) of adult *Tll4*-KO and wild-type C57BL/6J was collected either via cardiac puncture or from the tail vein into Eppendorf tubes containing 2 μ l of 10% EDTA or heparinized capillary tubes. RBC counts and indices were measured by an automated hematology analyzer (Celltac α ; Nihon Kohden, Tokyo, Japan) calibrated for mouse blood. For Giemsa staining, whole-blood smears were air-dried, methanol-fixed, and stained with Giemsa. Peripheral blood counts were also determined by diluting RBCs in RBC diluting fluid (3% sodium citrate, 1% Formalin) and then by manual counting using a hemocytometer. Reticulocytes were counted manually after staining with new methylene blue (Sigma-Aldrich). Images were acquired with an Olympus BX51 microscope equipped with an Olympus DP-72 camera (Tokyo, Japan).

Osmotic fragility and deformability analysis

Osmotic fragility was measured by the method of Gilligan et al. (1999). Whole blood was washed three times in isotonic buffer, and final hematocrit was adjusted to 5%. Diluted RBCs in a volume of 10 μ l were added to 290 μ l of lysis buffer of appropriate salt concentration and incubated for 20 min at room temperature. The lysed RBC suspension was then centrifuged, and the absorbance of the supernatant was measured at 540 nm. For measuring deformability, 30 μ l of whole blood was mixed with 4 ml of 3.5% polyvinylpyrrolidone solution, and the deformability index was recorded by increasing applied shear stress from 0 to 50 dynes/cm² using a custom-built ektacytometer.

RBC purification and preparation

We used three different methods to purify RBCs. RBCs were pelleted at 600 \times g for 10 min at 4°C. After removal of the plasma and top cell layer, including the buffy coat, the cells were washed six times in RBC wash buffer (5 mM ethylene glycol tetraacetic acid [EGTA], 0.25% NaCl, 5.0 mM Na₂HPO₄, pH 7.5). Second, for purification by FACS, whole blood was washed once with PBS, and then 10 μ l of blood was resuspended in FACS buffer (PBS, 0.5% bovine serum albumin [BSA], 1 mM EGTA, pH 7.5). The cell suspension was stained with TER-119 Alexa 488-conjugated antibody and then washed with PBS. Stained RBCs were sorted on a BD FACSAria (BD Biosciences, Franklin Lakes, NJ) and gated on the basis of their side scatter signals, forward scatter signals, and positive staining with TER-119 Alexa-488. The data were analyzed using FlowJo-V10 software. Third, a discontinuous gradient of 75% and 76.9% Percoll (Sigma-Aldrich) was used to separate RBCs.

Preparation of RBC membranes

To fractionate the soluble and membrane components of RBCs, washed RBCs were lysed with hypotonic buffer (20 mM Tris-Cl, 1 mM EGTA, pH 7.5), and the supernatant was separated by centrifugation. Next the cell pellet was washed repeatedly to remove all cytoplasmic content, and the final pellet consisting of RBC membrane ghosts was lysed directly in SDS-PAGE sample buffer, NP-40 lysis buffer, or RIPA buffer. The Mg²⁺ membrane ghosts and Triton-insoluble skeletons were prepared as described previously (Moyer *et al.*, 2010). Protein concentrations were measured using the BCA assay (Pierce, Rockford, IL). To determine the binding affinity of glutamylated and nonglutamylated NAP1 with the RBC membrane, Mg²⁺ membrane ghosts were treated with increasing concentrations (110, 210, and 310 mM) of KCl in a medium of lysis buffer (50 mM 4-(2-hydroxyethyl)-1-piperazineethanesulfonic acid, 1 mM MgCl₂, 1 mM EGTA, 1 mM dithiothreitol, 0.2% Triton X-100, 10% glycerol, pH 7.5) for 1.0 h and then centrifuged at 20,000 × *g* for 30 min at 4°C. After centrifugation, the supernatant was collected, and the remaining pellet was directly lysed in SDS-PAGE sample buffer.

Immunoprecipitation assay

To immunoprecipitate glutamylated proteins, mAb GT335 (Adipogen) was linked to protein G Sepharose beads (GE Healthcare, Little Chalfont, United Kingdom). For immunoprecipitation of NAP1L1, the anti-NAP1L1 antibody (Abcam) was linked to protein G Sepharose beads. The whole RBC lysate was added to the beads and incubated overnight at 4°C. Bound proteins were directly eluted in SDS-PAGE sample buffer.

Immunoblotting and immunofluorescence

SDS-PAGE was performed as described by Laemmli (1970). Fairbanks running buffer (Fairbanks *et al.*, 1971) was used to separate ankyrin from the spectrins. Gels were either stained with Coomassie blue or transferred to polyvinylidene fluoride membranes (Millipore) for immunoblotting. The membranes were probed with various primary antibodies, followed by horseradish peroxidase-conjugated secondary antibodies. Blots were developed with enhanced chemiluminescence reagents (ECL; GE Healthcare) and exposed in a Fuji Film Intelligent Dark Box (Tokyo, Japan), where the images were captured using Image Reader LAS-3000 software. For immunohistochemistry, RBC samples were washed three times with PBS (330 mOsm) containing 5 mM glucose, fixed for 20 min in 4% paraformaldehyde and 0.02% glutaraldehyde in PBS at room temperature, and rinsed three times in rinsing buffer (PBS containing 0.1 M glycine). Fixed cells were then permeabilized with PBS containing 0.1 M glycine and 0.1% Triton X-100 for 5 min at room temperature and again rinsed three times in PBS containing 0.1 M glycine. To ensure complete neutralization of the unreacted aldehydes, RBCs were then incubated in rinsing buffer at room temperature for 1.5 h. Nonspecific binding was blocked by incubation in blocking buffer (PBS containing 0.05 mM glycine, 0.2% BSA, and 5% goat serum) overnight at 4°C. After immunostaining, RBCs were allowed to attach to glass coverslips for 20 min in a humidified chamber and mounted on glass slides using Vectashield mounting medium for fluorescence (Vector Laboratories, Burlingame, CA) and observed by confocal laser scanning microscopy (FluoView FV1000; Olympus).

Ultrastructure studies

For SEM, whole blood was fixed with 2% glutaraldehyde in 0.1 M cacodylate buffer, pH 7.4, and postfixed in 1% OsO₄. Next the fixed cells were dehydrated, freeze-dried, and plasma-coated. The cells were photographed using a Hitachi S-4800 scanning electron micro-

scope. For TEM of the RBC membrane skeleton, copper grids of 400 mesh (Nissin-EM, Tokyo, Japan) were coated with 0.5% (wt/vol) Formvar in ethylene dichloride (Davison and Colquhoun, 1985) and then were carbon-coated and subjected to glow discharge (HDT-400 Hydrophilic Treatment Device; JEOL Datum, Tokyo, Japan). Collected blood cells were washed with PBS containing Mg and EGTA (Pi/NaCl/Mg; 150 mM NaCl, 5 mM NaH₂PO₄, 2 mM NaN₃, 2 mM MgCl₂, 1 mM EGTA, pH 5.5). Washed RBCs were then coated onto the grids as described by Byers and Branton (1985). Of note, the protocol by Byers and Branton (1985) is for spreading the RBC skeleton on the grid; however, our results (Figure 3A) indicate that the RBC membranes were not spread and remained at native mouse RBC size. TEM images of RBC membranes were obtained using a JEOL JEM-1220 transmission electron microscope with an accelerating voltage of 80 kV and equipped with a Gatan-Bioscan camera, Model 792 (Pleasanton, CA).

Image and statistical analyses

ImageJ software (<http://rsb.info.nih.gov/ij/index.html>) was used for densitometry analysis of Western blot data to measure the diameter of RBCs and for counting the holes in the RBC cytoskeleton. To calculate the coefficient of variance (CV), the means of RBC diameters acquired from each individual mouse were calculated. The mean diameters were used as representatives for each individual animal. The differences between the highest and lowest mean diameter of each genotype were used as values of variation. The coefficient of variance was calculated as $CV = \sigma/\mu$, where σ is SD and μ is mean diameter. To count the holes in the RBC membrane cytoskeleton, individual transmission electron micrographs were converted into binary format, plot profiles were measured, and the obtained peaks were counted manually. The histogram for RBC diameter was prepared in MATLAB. The significance of differences in the means was evaluated using the Student's two-tailed *t* test unless otherwise specified. $p < 0.05$ was considered significant. The results are expressed as mean ± SEM; *n* is the number of cells, and *N* is the number of animals.

ACKNOWLEDGMENTS

We thank Y. Ishimi (Ibaraki University, Mito, Japan) for providing the mAb 4A8 against NAP1, I. Ohta and Y. Kumakiri for technical assistance with electron microscopy experiments, K. Shibata for technical assistance with FACS, A. Konno for useful advice, and Y. Takakuwa and I. Koshino (Tokyo Women's Medical University, Tokyo, Japan) for conducting RBCs deformability experiments with an ektacytometer. We also thank N. Zaima and S. Akieda-Asai for their initial contributions to the analyses of *Ttl4*-KO mice. This work was supported in part by Grant-in-Aid for Challenging Exploratory Research 26670091 (to K.I.) and JSPS KAKENHI Grant Number JP15H05898B1 (to M.S.).

REFERENCES

- Boldface names denote co-first authors.
- Aguilar-Gurrieri C, Larabi A, Vinayachandran V, Patel NA, Yen K, Reja R, Ebong IO, Schoehn G, Robinson CV, Pugh BF, Panne D (2016). Structural evidence for Nap1-dependent H2A–H2B deposition and nucleosome assembly. *EMBO J* 35, 1465–1482.
- Andrews AJ, Chen X, Zevin A, Stargell LA, Luger K (2010). The histone chaperone NAP1 promotes nucleosome assembly by eliminating non-nucleosomal histone DNA interactions. *Mol Cell* 37, 834–842.
- Becker PS, Morrow J, Lux SE (1987). Abnormal oxidant sensitivity and beta-chain structure of spectrin in hereditary spherocytosis associated with defective spectrin-protein 4.1 binding. *J Clin Invest* 80, 557.

- Byers TJ, Branton D (1985). Visualization of the protein associations in the erythrocyte membrane skeleton. *Proc Natl Acad Sci USA* 82, 6153–6157.
- Chen H, Khan AA, Liu F, Gilligan DM, Peters LL, Messick J, Haschek-Hock MW, Li X, Ostafin AE, Chishti AH (2007). Combined deletion of mouse dematin-headpiece and beta-adducin exerts a novel effect on the spectrin-actin junctions leading to erythrocyte fragility and hemolytic anemia. *J Biol Chem* 282, 4124–4135.
- Chen Z, Naveiras O, Balduini A, Mammoto A, Conti MA, Adelstein RS, Ingber D, Daley GQ, Shivdasani RA (2007). The May-Hegglin anomaly gene MYH9 is a negative regulator of platelet biogenesis modulated by the Rho-ROCK pathway. *Blood* 110, 171–179.
- Davison E, Colquhoun W (1985). Ultrathin formvar support films for transmission electron microscopy. *J Electron Microscop Tech* 2, 35–43.
- Edde B, Rossier J, Le Caer JP, Desbruyeres E, Gros F, Denoulet P (1990). Posttranslational glutamylation of alpha-tubulin. *Science* 247, 83–85.
- Fairbanks G, Steck TL, Wallach DF (1971). Electrophoretic analysis of the major polypeptides of the human erythrocyte membrane. *Biochemistry* 10, 2606–2617.
- Fibach E, Rachmilewitz E (2008). The role of oxidative stress in hemolytic anemia. *Curr Mol Med* 8, 609–619.
- Fowler VM (2013). The human erythrocyte plasma membrane: a Rosetta Stone for decoding membrane - cytoskeleton structure. *Curr Top Membr* 72, 39–88.
- Gilligan DM, Lozovatsky L, Gwynn B, Brugnara C, Mohandas N, Peters LL (1999). Targeted disruption of the beta adducin gene (*Add2*) causes red blood cell spherocytosis in mice. *Proc Natl Acad Sci USA* 96, 10717–10722.
- Gokhin DS, Nowak RB, Khoory JA, de la Piedra A, Ghiran IC, Fowler VM (2015). Dynamic actin filaments control the mechanical behavior of the human red blood cell membrane. *Mol Biol Cell* 26, 1699–1710.
- Ikegami K, Heier RL, Taruishi M, Takagi H, Mukai M, Shimma S, Taira S, Hatanaka K, Morone N, Yao I, et al. (2007). Loss of alpha-tubulin polyglutamylation in ROSA22 mice is associated with abnormal targeting of KIF1A and modulated synaptic function. *Proc Natl Acad Sci USA* 104, 3213–3218.
- Ikegami K, Mukai M, Tsuchida J, Heier RL, MacGregor GR, Setou M (2006). TTL7 is a mammalian beta-tubulin polyglutamylase required for growth of MAP2-positive neurites. *J Biol Chem* 281, 30707–30716.
- Ikegami K, Setou M (2010). Unique post-translational modifications in specialized microtubule architecture. *Cell Struct Funct* 35, 15–22.
- Italiano JE, Patel-Hett S, Hartwig JH (2007). Mechanics of proplatelet elaboration. *J Thromb Haemost* 5, 18–23.
- Janke C, Rogowski K, Wloga D, Regnard C, Kajava AV, Strub JM, Temurak N, van Dijk J, Boucher D, van Dorsselaer A, et al. (2005). Tubulin polyglutamylase enzymes are members of the TTL domain protein family. *Science* 308, 1758–1762.
- Kalfa TA, Pushkaran S, Mohandas N, Hartwig JH, Fowler VM, Johnson JF, Joiner CH, Williams DA, Zheng Y (2006). Rac GTPases regulate the morphology and deformability of the erythrocyte cytoskeleton. *Blood* 108, 3637–3645.
- Kashiwaya K, Nakagawa H, Hosokawa M, Mochizuki Y, Ueda K, Piao LH, Chung SY, Hamamoto R, Eguchi H, Ohigashi H, et al. (2010). Involvement of the tubulin tyrosine ligase-like family member 4 polyglutamylase in PELP1 polyglutamylation and chromatin remodeling in pancreatic cancer cells. *Cancer Res* 70, 4024–4033.
- Kaushansky K (2008). Historical review: megakaryopoiesis and thrombopoiesis. *Blood* 111, 981–986.
- Klimchenko O, Mori M, DiStefano A, Langlois T, Larbret F, Lecluse Y, Feraud O, Vainchenker W, Norol F, Debili N (2009). A common bipotent progenitor generates the erythroid and megakaryocyte lineages in embryonic stem cell-derived primitive hematopoiesis. *Blood* 114, 1506–1517.
- Laemmli UK (1970). Cleavage of structural proteins during the assembly of the head of bacteriophage T4. *Nature* 227, 680–685.
- Liu J, Guo X, Mohandas N, Chasis JA, An X (2010). Membrane remodeling during reticulocyte maturation. *Blood* 115, 2021–2027.
- Liu SC, Derick LH, Palek J (1987). Visualization of the hexagonal lattice in the erythrocyte membrane skeleton. *J Cell Biol* 104, 527–536.
- Lux SE 4th (2016). Anatomy of the red cell membrane skeleton: unanswered questions. *Blood* 127, 187–199.
- Miller KE, Heald R (2015). Glutamylation of Nap1 modulates histone H1 dynamics and chromosome condensation in *Xenopus*. *J Cell Biol* 209, 211–220.
- Mohandas N, Gallagher PG (2008). Red cell membrane: past, present, and future. *Blood* 112, 3939–3948.
- Moyer JD, Nowak RB, Kim NE, Larkin SK, Peters LL, Hartwig J, Kuypers FA, Fowler VM (2010). Tropomodulin 1-null mice have a mild spherocytic elliptocytosis with appearance of Tropomodulin 3 in red blood cells and disruption of the membrane skeleton. *Blood* 116, 2590–2599.
- Onikubo T, Nicklay JJ, Xing L, Warren C, Anson B, Wang WL, Burgos ES, Ruff SE, Shabanowitz J, Cheng RH (2015). Developmentally regulated post-translational modification of nucleoplamin controls histone sequestration and deposition. *Cell Rep* 10, 1735–1748.
- Park YJ, Luger K (2006). The structure of nucleosome assembly protein 1. *Proc Natl Acad Sci USA* 103, 1248–1253.
- Qu Y, Hahn I, Webb SED, Pearce SP, Prokop A** (2017). Periodic actin structures in neuronal axons are required to maintain microtubules. *Mol Biol Cell* 27, 296–308.
- Regnard C, Desbruyeres E, Huet JC, Beauvallet C, Pernollet J, Edde B (2000). Polyglutamylation of nucleosome assembly proteins. *J Biol Chem* 275, 15969–15976.
- Salomao M, Zhang X, Yang Y, Lee S, Hartwig JH, Chasis JA, Mohandas N, An X (2008). Protein 4.1 R-dependent multiprotein complex: new insights into the structural organization of the red blood cell membrane. *Proc Natl Acad Sci USA* 105, 8026–8031.
- Seebart C, Prenni J, Tomschik M, Zlatanova J (2010). New nuclear partners for nucleosome assembly protein 1: unexpected associations. *Biochem Cell Biol* 88, 927–936.
- Shi ZT, Afzal V, Collier B, Patel D, Chasis JA, Parra M, Lee G, Paszty C, Stevens M, Walensky L, Peters LL (1999). Protein 4.1 R-deficient mice are viable but have erythroid membrane skeleton abnormalities. *J Clin Invest* 103, 331–340.
- Swihart AH, Mikrut JM, Ketterson JB, Macdonald RC (2001). Atomic force microscopy of the erythrocyte membrane skeleton. *J Microscop* 204, 212–225.
- Van Dijk J, Miro J, Strub JM, Lacroix B, Van Dorsselaer A, Edde B, Janke C (2008). Polyglutamylation is a post-translational modification with a broad range of substrates. *J Biol Chem* 283, 3915–3922.
- Van Dijk J, Rogowski K, Miro J, Lacroix B, Edde B, Janke C (2007). A targeted multienzyme mechanism for selective microtubule polyglutamylation. *Mol Cell* 26, 437–448.
- Vannucchi AM, Paoletti F, Linari S, Cellai C, Caporale R, Ferrini PR, Sanchez M, Migliaccio G, Migliaccio AR (2000). Identification and characterization of a bipotent (erythroid and megakaryocytic) cell precursor from the spleen of phenylhydrazine-treated mice. *Blood* 95, 2559–2568.
- Ye BQ, Li C, Yang Z, Wang YY, Hao JF, Wang L, Li Y, Du Y, Hao L, Liu BY, et al.** (2014). Cytosolic carboxypeptidase CCP6 is required for megakaryopoiesis by modulating Mad2 polyglutamylation. *J Exp Med* 211, 2439–2454.
- Zlatanova J, Seebart C, Tomschik M (2007). Nap1: taking a closer look at a juggler protein of extraordinary skills. *FASEB J* 21, 1294–1310.